Oxidation of a chromia-forming nickel base alloy at high temperature in mixed diluted CO/H2O atmospheres

Fabien Rouillard, Céline Cabet, Krzysztof Wolski, Michèle Pijolat

Corrosion Science, 2009, 51(4), 752-760, doi:10.1016/j.corsci.2009.01.019

Oxidation of a chromia-forming nickel base alloy at high temperature in mixed diluted CO/H_2O atmospheres

ROUILLARD[A], F .; CABET[A], C. ; WOLSKI[B], K. ; PIJOLAT[B], M.

[A]CEA, DEN, DPC, SCCME, Laboratoire d'Etude de la Corrosion Non Aqueuse, 91191 Gif sur Yvette, France
[B]Ecole Nationale Supérieure des Mines, MPI – CNRS UMR5146 – Centre SMS, 158 Cours Fauriel, 42023 Saint Etienne, France
[C]Ecole Nationale Supérieure des Mines, LMPG – CNRS UMR5148 – Centre SPIN, 158 Cours Fauriel, 42023 Saint Etienne, France
mpijolat@emse.fr ; wolski@emse.fr

Abstract

Corrosion of a chromia-forming nickel base alloy, Haynes 230_, has been investigated under impure helium containing a few Pa of CO and H_2O at 900 °C. It has been found that this alloy reacts simultaneously with CO and H_2O. Oxidation by CO has been revealed to occur mainly in the first hours. CO diffuses through the scale via short-circuit pathways and oxidizes Al, Cr and Si at the oxide/metal interface. Kinetics of CO oxidation has been investigated and several rate limiting steps are proposed. In the long term, H_2O is the major oxidant of chromia-forming nickel base alloys in impure helium.
Keywords : *Superalloys ; SIMS ; High temperature Corrosion ; Oxidation; Reactor conditions*

Introduction

High temperature oxidation behaviour of alloys in mixed gas environments has been one of the major scientific and engineering interests in the large field of environmentally induced degradation of materials over the past 15 years [1–3]. High Temperature gas cooled Reactor (HTR) is a nuclear system with an all graphite core where a mixed gas environment can be found. The helium coolant contains small amounts of impurities typically H_2, H_2O, CO, and CH_4. The challenge here is that the atmosphere is highly diluted [4]. Even if their partial pressures are only between a few tens to hundreds of Pa, the gas impurities can react at high temperature with metallic materials, in particular with the chromia-forming alloys for heat exchanger. Gas–metal interactions involved in HTR have been discussed in numerous papers published in the past three decades [5–12] and more recently in France [13–16]. These works have demonstrated that depending on the composition of the chromia-forming alloy, on the working temperature (850–1000 °C) and on the partial pressures of gas species in helium, two main behaviours could be distinguished: either a passive corrosion based on the formation of a stable, slow-growing, Cr rich oxide layer on the surface or an active corrosion with the destruction of the surface oxide layer and the subsequent decarburization or carburization of the alloy [14]. Haynes 230® is a good candidate alloy for HTR heat exchanger.It has been shown [13,14] that Haynes 230® forms a Mn–Cr rich oxide layer at 900 °C under a helium atmosphere with 20 Pa H_2, 2 Pa CH_4, 5 Pa CO and 0.15 Pa H_2O. The purpose of the present work is to describe the oxide growth at 900°C under this mixed oxidizing environment with CO and H_2O. The composition and morphology of the oxide layer have been accurately analysed. The influence of the water vapour content in helium and the influence of the alloy composition on CO reactivity have been investigated using an evolved gas analysis technique. Moreover two-stage experiments under helium mixture without then with $^{13}C^{18}O$ have been carried out to precise where is localized the interface of CO reaction. These results combined with accurate analyses of the nature and the morphology of the oxide layer has allowed a better understanding of the kinetics of CO consumption in the HTR conditions.

Experimental

Materials

Haynes 230® was provided by Haynes Int.® in the plate form, annealed at 1230 °C for 10 min then water quenched. A model alloy Ni–22Cr–14W–0.1C was provided by the *SMS Centre of the Ecole Nationale Supérieure des Mines de St Etienne*. Its chemical composition is based on Haynes 230® but it only contains the major elements.It was prepared by electromagnetic melting in cold crucible of a Ni–30Cr ingot with W rods, Ni billets and carbon powder to yield the nominal composition. After casting, the ingot was hot worked at 1260 °C to obtain a rod with a diameter of 18 mm. A 1.5 mm-thick layer was machined off the surface to remove the decarburized zone. Then, the rod was annealed under argon at 1350 °C for 10 h then at 1100 °C for 14 h in order to obtain a homogeneous precipitation of $M_{23}C_6$ carbides. Finally, it was water quenched. Haynes 230®and model alloy were cut into rectangular specimens of approximate dimensions 25 × 12 × 2 mm. They were polished down to a 1 μm finish, ultrasonically degreased in an acetone– ethanol mixture and weighed.
The chemical composition of both alloys is presented in Table 1. The carbon content was analysed by combustion coupled with absorption spectroscopy (LECO®). Haynes 230®composition was obtained by Inductively Coupled Plasma (ICP) after the alloy was dissolved in acid.

Oxidation tests

Oxidation tests were carried out under atmospheric pressure using the gas mixtures described in Table 2. Two specimens were exposed to the flowing gas in a quartz tube reactor inserted in a high temperature furnace. They were heated at a rate of 1 °C/min then maintained at 900 °C (850 °C for test E). After exposure, the samples were cooled at a rate of 2.5 °C/min under pure helium. At the quartz tube outlet, the gas was analysed by Gas Phase Chromatography (GPC) with a helium detector. The time between two analyses was 10 min. In order to check if the relative change in gas concentrations is representative of gas/metal reactions, a blank test was carried out without any specimen. Fig. 1 shows that no gas/gas reaction occurred below 950 °C whereas thermodynamic allows the reaction (1) to occur at high temperature:

$$CH_4 + H_2O \rightarrow CO + 3H_2 \quad (1)$$

The results are shown in Fig. 1. It is probably due to the very low partial pressures of gas impurities in helium which prevents the molecules to interact perfectly and consequently the thermodynamic equilibrium to be established.

2.3. Methods of surface analysis

The corrosion products were analysed by Field Emission Scanning Electron Microscopy, microprobe, Transmission Electron Microscopy (TEM), X-Ray Diffraction (XRD), X-Ray Photoelectron Spectroscopy (XPS) and Glow Discharge Optical Emission Spectroscopy (GDOES). Details on the different apparatus and analysis conditions are given in [14]. After test E (see Table 2), the distribution of the ^{13}C isotope was analysed in the surface scale by Glow Discharge Mass Spectroscopy (GDMS) using a VG9000 spectrometer. The oxide composition as well as the distribution of the oxygen isotope were determined by Ar^+-SIMS using a CAMECA Riber MIQ256 secondary ion mass spectrometer.

Experimental results

3.1. Gas phase analyses

Fig. 2 shows the relative change in the CO partial pressure between the outlet and the inlet of the furnace. Due to reaction with the specimens, CO was consumed during the

heating up. CO consumption started at around 650 °C in test B with P_{H_2O} = 0.16 Pa and this temperature increased with the water vapour content in helium up to 850 °C in test A with P_{H_2O} = 0.4 Pa. In both experiments, the rate of consumption increased with increasing temperature and reached its maximum at 900 °C. Then, at constant temperature, the reaction rate decreased with time. After roughly 15 h, the reaction rate fell down below the detection limit of the GPC which is about 10^{-12} mol/s. The area under the peak in Fig. 2 gives information about the total quantity of CO having reacted. The methane partial pressure difference between the inlet and the outlet of the furnace was too low to be measured. As a consequence, methane reactivity with the specimens was considered to be negligible at 900 °C. Fig. 2 also gives the gas phase analysis for the Ni–22Cr–14W– 0.1C specimens which did not contain any minor alloying elements. The model alloy did not show any significant reactivity with CO. This observation strongly suggests that CO mainly reacted with the minor elements of Haynes 230® such as Al and Si.

3.2. Analyses of the corrosion products

An accurate description of the oxide layer was obtained by combining microprobe analysis, grazing XRD analysis at 1° and EDXS/TEM analysis. Figs. 3–5 show oxide scales formed on Haynes 230® after respectively test A and B. Results of different EDXS analyses performed in Fig. 5 are given in Table 3. The oxide layer can be decomposed in two main parts: an upper continuous film and inner nodules. The outer part of the continuous film (spots 1 and 2) was analysed to be Mn/Cr rich oxide (JCPDS No.: 00-006-0504) whereas the inner part (spot 3) was only pure chromia (JCPDS No.: 01-071-0982). The nodules (spot 6) were mainly Cr and Al rich oxides. An aluminium and silicon enrichment was also revealed in the area between the oxide layer and the nodules (spots 4 and 5). Finally, intergranular Al rich oxides were formed deeper in the alloys.
In Fig. 3, the white inclusion was a M_6-type carbide – with M being mainly W and Cr – initially present in the alloy. It can be assumed that this particle has been cut during the initial preparation of the sample. Thus, its flat top should roughly materialize the original alloy surface. Considering this assumption, the interface between the oxide layer and the inner nodules should approximately correspond to the original surface. This is in good agreement with the presence of aluminium and silicon at this interface (see Section 4) since silicon and aluminium oxidized on the surface during the very first stages of oxidation as shown by XPS analysis of a Haynes 230® specimen heated at 950 °C (1°C/min) under helium with a reduced content of oxidizing species.

3.3. Carbon profile at the surface of Haynes 230®

Using a thorough calibration method, GDOES made it possible to obtain a quantitative profile of carbon through Haynes 230® surface after test C. Fig. 5 presents the mass fraction of carbon as a function of sputtering time.
In Fig. 6 the interface between the oxide and the alloy could be located thanks to the inflexion point of the O profile (not represented). The profile indicates that carbon accumulated underneath the oxide surface and progressive decreased down to the as-received level in the alloy. By considering a sputtering rate equal to 7 μm/min in the prevailing conditions of the GDOES analysis, carbon may have diffused into the alloy bulk over approximately 25 *m. In Fig. 6, the area delimited by the oxide/alloy interface (the vertical dotted line), the initial carbon content (the horizontal dotted line) and the carbon profile gives the carbon content transferred into the alloy during the test. On the other hand, the area under the peak in Fig. 2 corresponds to the amount of CO which concurrently reacted. These two data are reported in Table 4. The amount of carbon found under the oxide layer is in good agreement with the amount of CO which has been

consumed (±6%) as expected from Fig. 2 which shows that the reactivity of methane was negligible.

3.4. Influence of CO and H_2O on the oxide layer morphology

Table 5 presents the mean thickness of the oxide layer formed after test A (Fig. 3) and test B (Fig. 4) as estimated by FESEM imaging. Besides, GPC analyses (cf. Fig. 2) allowed calculating the total consumption of CO during the tests. These data correspond to a given amount of oxygen transferred to the oxide that eventually can be used to estimate the thickness of oxide produced only by CO – with the assumption that the entire oxide layer was Cr_2O_3 (molar volume = 28.1 cm^3) (see Table 5). Finally, the last column compares the two results in terms of fraction of the oxide layer due to oxidation by CO. It underlines an important result: the higher the water vapour content in helium, the thicker the oxide layer and the lower the CO percentage that reacts with the alloy. Thus CO and H_2O were in competition with respect to the oxidation of the alloy. Besides, it is worth noticing that the oxide layer morphology shown in Figs. 3 and 4 is different: after test B which contained the lower water vapour content (0.16 Pa), the upper continuous layer was thinner than after test A richer in water vapour (0.4 Pa). Moreover, the inner rough oxide was more pronounced after test B.

Discussion

4.1. Oxide nature and structure

Expositions of Haynes 230® specimens at 900 °C under impure helium, typically 2–5 Pa CO – 0–2 Pa CH_4 – 20 Pa H_2 and 0.01–0.4 Pa H_2O, have showed the growth of a continuous chromium rich oxide layer on the alloy surface (see Fig. 3). Its upper part is enriched with manganese, forming a spinel $Mn_xCr_{(3-x)}O_4$ phase (see Fig. 5 and Table 3). The chemical composition of this oxide layer is identical to that of the oxide formed on Haynes 230® at high temperature in air [18] and is similar to that of other chromium rich nickel base alloys containing a small quantity of manganese when exposed in oxidizing atmospheres [8]. The strong tendency for Mn to concentrate in the outer area of the scale is said to be related to a diffusion coefficient of Mn ions hundred times larger than that of Cr ions in chromia at 900 °C [19].

At the very first steps of exposition, it has been shown that Al and Si start to oxidize and concentrate discontinuously at the original alloy surface. This observation has already been noted on Haynes 230® oxidized in air at high temperature [18]. The presence of these oxidized elements on the surface could be explained by two main reasons: first, the segregation energy is favoured on Haynes 230® [20] and secondly, the driving force for their oxidation is higher than for the other elements (Cr and Mn particularly). However, because their content is very low in Haynes 230® (0.3– 0.4 wt%), the growth of Al and Si rich oxides is limited and Mn/Cr rich oxide starts to grow over them. At longer times, Al rich oxides can still be formed deeper in the alloy, particularly at grain boundaries, where the chemical potential of oxygen set by the dissociation pressure of Cr_2O_3 is high enough to oxidize aluminium.

4.2. Oxidation reactions by H_2O and CO

As already suggested [5, 11, 14, 21], Table 5 shows that the oxide layer formation is due to reactions with H_2O and CO according to (2) and (3):

$$\chi M + yH_2O = M\chi Oy + yH_2(g) \quad (2)$$

$$\chi M + yCO = M\chi Oy + yC_{solution} \quad (3)$$

where M = Al, Cr, Mn, Si and $C_{solution}$ represents carbon dissolved in the alloy matrix.

A competition between H_2O and CO has been evidenced in Table 4: the higher the water vapour in helium, the lower the probability for CO molecules to react on the surface.

Moreover, differences in the reactivity of CO and H_2O may be explained by considering the thermodynamic and kinetic of the reactions. Fig. 7 shows that the standard free Gibbs energy of oxidation of Cr by CO strongly depends on Cr activity whereas oxidation by H_2O depends a little on a_{Cr}: at 900 °C, Cr did not react with CO below an activity of about 0.4 but still react with H_2O even when chromium activity is as low as to 0.01. Consequently, Cr_2O_3 may be formed in the beginning by reactions with both CO and H_2O. Then as far as the Cr activity near the oxide/alloy interface decreases, oxidation by CO is less and less possible.
As carbon from CO was transferred beneath the oxide scale (see Fig. 6 and Table 4), it is very likely that CO reacted at the oxide/alloy interface. It is assumed that diffusion occurred via short-circuit pathways. CO molecules then should be dissociated at the oxide/alloy interface leading simultaneously to oxide growth and deposition of carbon. Moreover the industrial alloy containing minor elements like Al and Si consumed more CO than the model alloy as shown in Fig. 2. Fig. 8 shows that from a thermodynamic point of view, CO preferentially oxidizes Al and Si over Cr in Haynes 230® even if their activities are much smaller. However, because Al and Si contents are limited in Haynes 230®, they do not uniformly oxidize on the surface but rather form small localized nodules. This non uniform precipitation could explain the geometry of the rough inner oxide: Cr cannot be oxidized under areas where Al rich nodules are formed since Al/Al_2O_3 equilibrium imposes a too low partial pressure of oxygen whereas Cr does oxidize in areas between nodules.
On the other hand, the outer Cr rich oxide layer should mainly be due to oxidation by water vapour according to a mechanism which involves H_2O dissociation at the surface of Cr_2O_3 and bulk Cr^{3+} diffusion through the scale. Comparison of the molecule radius of H_2O to CO which is respectively 96 pm and 111 pm shows that the water vapour is smaller than carbon monoxide and one can thus expect that it will diffuse faster than CO through the oxide layer and participate actively to the inward part of the oxide layer. It is not what our results reveal. In fact, in VHTR environment, the water vapour partial pressure in helium is always very low (few Pa) and as a consequence most of water molecules reacts at the gas/oxide interface as soon as it is adsorb on the oxide surface. Like CO, some water molecules may also diffuse in high diffusion pathways through the oxide layer but their participation to the inner oxide compared to the one done by CO is negligible because the ratio P_{CO}/P_{H2O} is high (>>10).

4.3. Specific reactivity of CO

To verify if the inner oxide nodules could be mainly formed by oxidation with CO, the two-stage oxidation experiment E was carried out on model Ni–22Cr–14W–0.1C alloy at 850 °C **{1}**

- In the first step, two samples were exposed to a He mixture with 8–10 Pa $H_2{}^{16}O$ /200 Pa H_2. A compact oxide layer should grow only containing ^{16}O.
- Then the same samples were exposed to a dry He mixture with 5 Pa $^{13}C{}^{18}O$ (H_2O < 0.01 Pa) without decreasing neither the temperature nor the H_2 partial pressure. During this second step, $^{13}C{}^{18}O$ is the only species able to react.

The main purpose of test E was to localize the site where CO reacts via the respective positions of ^{13}C and ^{18}O profiles versus ^{16}O profile. After the two-step experiment E, the oxide layer was observed by SEM and its structure and nature revealed to be identical to the one showed in Fig. 3. Fig. 9 shows SIMS profiles of ^{16}O, ^{18}O and ^{52}Cr through the alloy surface after test E and Fig. 10 presents the complementary profiles of ^{13}C and ^{16}O obtained by GDMS. The two dotted vertical lines in Figs. 9 and 10 represent the inflexion points of ^{16}O and ^{52}Cr signals and should thus materialize the border lines of the oxide/alloy interface. In Figs. 9 and 10, ^{18}O and ^{13}C present quite a similar profile from the

outside to the alloy bulk: a decreasing slope through the pre-formed continuous oxide layer made of ^{16}O, then an accumulation near the oxide/alloy interface. Nevertheless, it has to be noted that the intensity level of ^{18}O signal is hundred times lower than that of ^{16}O signal meaning that CO did react with the Ni–22Cr–14W–0.1C specimens during the second step but not significantly. The fact that ^{13}C and ^{18}O signals follow the same profile through the oxide layer strongly supports that the diffusing species may be CO. This result agrees with our previous assumption that CO should directly react with the metal at the oxide/alloy interface.

The two-stage oxidation test E was carried also out for Haynes 230®. The SIMS profiles were similar confirming that very few CO molecules reacted at the oxide/alloy interface. According to Basu *et al.* [24], the shape of ^{13}C (and CO) profile is typically representative of a profile of a specie reacting at the oxide/alloy interface and diffusing along short-circuit pathways such as oxide grain boundaries. Permeability of gas through seemingly compact oxide layers has been discussed in a lot of papers [25–28]. It more often calls for gas diffusion into cracks developed in the oxide layer even if such cracks have never been evidenced so far. Recently, Young et al. [1– 3], who have worked on oxidation in mixed gas atmospheres, typically $CO/CO_2/N_2$ and $CO/CO_2/SO_2/N_2$ observed the penetration of carbon bearing molecules through chromia even though any crack was evidenced and though carbon solubility in Cr_2O_3 is known to be negligible [29]. They proposed that molecular transport of gas species could occur into the oxide along internal surfaces such as oxide grain boundaries and so called nanochannels or nanopores as surface diffusion at the surface of such nanochannel may be preponderant on the Knudsen diffusion of gas molecules – if the size of the nanochannel is not much higher than that of molecules. According to the conclusions of Young et al. and respect to our SIMS results, CO may also be transferred through the surface chromia layer of NiCrW and Haynes 230® via molecular transport through nanochannels.

4.4. Kinetics of CO reaction

It was previously evidenced that CO reacts at the inner interface, presumably with Al, Si and Cr to a less extent. Upon edification of the oxide layer, both the available surface for reaction with CO at the oxide/alloy interface and the activity of oxidizable elements decrease. The consumption rate of CO is thus expected to decrease with time as it is actually observed in Fig. 2. After roughly 15 h, the difference between the outlet P_{CO} and the inlet P_{CO} falls below the detection limit of GPC which is 10^{-12} mol/cm^2/s. At this time, the oxide layer appears to be compact on FESEM images (see Fig. 3). A basic approach would argue that after 15 h, CO does not react anymore because of the growth of a perfectly impermeable oxide layer which totally prevents CO from accessing to the oxide/alloy interface. However, SIMS combined to GDMS analyses after test E (see Figs. 9 and 10) discredits this scenario: even after the formation of a continuous compact oxide layer (~500 nm), some CO can still diffuse through the oxide layer and react at the oxide/alloy interface. The reaction rate is not nul but very low (<10^{-12} mol/cm^2/s).

In the following, the kinetic of CO reaction after the formation of a seemingly compact oxide layer (~15 h) is investigated by comparing the rate of involved processes to the consumption rate: diffusion of CO through the oxide layer, reaction of CO at the oxide/alloy interface or bulk diffusion of oxidizing element to the oxide/alloy interface. On one hand, it has been observed [30] that CO can be released and transported fast through the scale (8.10^{-12} mol/cm^2/s) because of a specific reaction between oxide and carbon in solution at the oxide/alloy interface. Since the surface diffusion rate of CO through oxide grain boundaries or nanochannels is much too low to explain such a high rate of CO release, faster ways of diffusion such as gas diffusion in nanochannels must exist as well. As discussed in [30], this nanochannel network may have been constituted

during the oxide growth. The rate of CO diffusion through the scale (8.10^{-12}mol/cm²/s) is thus far higher than the rate of CO reaction and might no be rate limiting.
Mention should mades that high diffusion paths with a predominant gas diffusion through the oxide layer usually influences the SIMS/GDMS profiles after two-stage experiments. According to Basu *et al.* [24], an accumulation at the oxide/alloy interface and an almost flat profile in the old oxide layer would be expected which is quite different from what has been observed on Figs. 8 and 9. A possible reason could be that only very few quantities of CO would have reacted at the oxide/metal interface after the second stage of test E due to the depletion of reactive elements during the first stage.
On the other hand, it has been previously evidenced that CO preferentially reacts with Al (see Fig. 8). One could estimate the Al supply at the oxide/alloy interface. Fig. 10 presents the Al profiles obtained by GDOES below the oxide layer formed on Haynes 230® after tests C (25 h) and D (6 h). The alloy is depleted in Al near the oxide/alloy interface and Al concentration near this interface decreases with time. This decrease may reflect a mixed kinetic. With the assumption that Al concentration at the oxide/alloy interface is negligible beside the bulk one, it is possible to calculate the upper limit flow of Al to the oxide/alloy interface by the Fick relationship in a semi-infinite solid [31]:

$$J_{Al} = D_{Al}\frac{[Al]^0}{\sqrt{\pi D_{Al} t}} \quad (4)$$

with $[Al]^0$ the bulk Al concentration, t the holding time at 900 °C and D_{Al} the diffusion coefficient of Al in Haynes 230® at 900 °C.
D_{Al} can be determined by fitting the Al profiles in Fig. 11 with Eq. (5) [31]:

$$\frac{[Al]^{\chi} - [Al]^0}{[Al]^i - [Al]^0} = erf\left(\frac{\chi}{2\sqrt{D_{Al} t}}\right) \quad (5)$$

in which χ is the depth in cm, [Al] the Al concentration at x in mol/cm³ and $[Al]^i$ the Al concentration at the oxide/alloy interface.
Eq. (5) fits well the two profiles with correlation coefficients equal to 0.99. The diffusion coefficients of Al obtained from C and D are, respectively, 3.10^{-13}cm²/s and 5.10^{-13} cm²/s. These values are of the same order of magnitude than D_{Al} in pure Ni at 850°C (approximately 6.5×10^{-13}cm²/s [21]).
By taking a mean value for D_{Al} = 4.10^{-13}cm²/s at 900°C and with $[Al]^0$ =$1.2.10^{-3}$ mol/cm³ and t = 54,000 s (15 h), the relation (4) gives: $J_{Al} \cong 1.8.10^{-12}$ mol/cm²/s.
CO would only react with Al where the molecules can reach the oxide/alloy interface via the previously discussed high diffusion paths. By taking into account one tube-like nanochannel per grain with a cross section A and oxide grains with a mean diameter Φ, the flow of CO consumption would become:

$$J_{CO} \approx \frac{3}{2}\frac{J_{Al} A}{\Phi^2} \quad (6)$$

if the diffusion rate of aluminium in the alloy is the rate limiting step of CO consumption, that is to say that J_{CO} is roughly equal to 10^{-12}mol/s/cm². After Eq. (6) with Φ equal to 60 nm which is themean diameter of the oxide grains assessed by TEM observations, the diameter of the nanochannels has to be equal to 40 nm. This size is too large since the oxide layer appears already compact at this time when observed by TEM. In fact, smaller nanochannels have to be assumed but then, the Al flow to the oxide/alloy interface below them is too low to explain the whole CO reaction. As a consequence Al diffusion to the

oxide/alloy interface cannot be the only rate limiting step of CO reaction: Si and Cr may react with CO to a certain extent as well and their diffusion to the oxide/alloy interface may participate to rate limiting step of CO reaction.

Conclusion

At 900 °C under impure helium containing few amounts (ppm) of CO and H_2O, chromia-forming nickel based alloy, Haynes 230®, develops an upper Mn–Cr rich oxide layer with an inner discontinuous Al oxides. It has been shown by classical then "double oxidation" experiments that CO reacts mainly during the early time of exposition (a few hours) and that this reaction mainly occurs at the oxide-metal interface. Transport through the scale is likely to occur through oxide grain boundaries and/or nanochannels. After a few hours, H_2O becomes the major oxidant. As a consequence, it will control the long term oxidation behaviour of the alloy. In the meantime, CO can always access to the oxide/metal interface but the oxidation by CO becomes very low and the possible rate limiting steps have been quantitevely investigated. It has been proposed that the reaction of CO with the oxidizable elements Al, Si and Cr at the oxide/metal interface actually limits the reaction rate.

{1} The test was carried at 850°C because it has been evidenced in [14] that the oxide layer suffered from reduction by carbon in solution in the alloy when specimens were exposed at 900°C in helium atmosphere without any CO and containing low partial pressure of water vapour.

Acknowledgements

The authors are thankful to Mme M.C. Lafont at the Université Paul Sabatier of Toulouse for performing TEM analyses, to Mr P.Bonnaillie for the FESEM pictures performed at the CEA/DEN/DANS/DMN/SRMP, to Pr. S. Chevalier and Dr. O. Heintz for the SIMS analyzes performed at the Institute Carnot of Bourgogne and to Mr. M. Tabarant for the GDOES and the GDMS analyses performed at the CEA/DEN/DANS/DPC/SCP/LRSI.

References

[1] X. G Zheng, D.J. Young, High temperature corrosion of Cr_2O_3-forming alloys in $CO–CO_2–N_2$ atmospheres, Oxid. Met. 42 (3/4) (1994) 163–190.
[2] D.J. Young, S. Watson, High-temperature corrosion in mixed gas environments, Oxid. Met. 44 (1/2) (1995) 235–264.
[3] D.J. Young, Simultaneous oxidation and carburisation of chromia formingalloys, Int. J. Hydrogen Energy 32 (2007) 3763–3769.
[4] L.W. Graham, M.R. Everett, D. Lupton, F. Ridealgh, D.W. Sturge, M. Wagner-Löffler, Environmental conditions in HTRs and the selection and developmentof primary circuit materials, in: Proceedings of a Symposium Jülich, IAEA, Vienna, 1976, pp. 319–352.
[5] K.G.E. Brenner, Ternary diagrams for the characterization of metallic corrosion in high-temperature reactors, Gas Cooled Today, BNES, London, 1982.
[6] K.G.E. Brenner, L.W. Graham, The development and application of a unified corrosion model for high temperature gas-cooled reactor systems, Nucl.Technol. 66 (1983) 404–414.
[7] H.J. Christ, U. Künecke, K. Meyer, H.J. Sockel, High-temperature corrosion of the nickel-based alloy Inconel-617 in helium containing small amounts of impurities, Mater. Sci. Eng. 87 (1987) 161–168.
[8] M. Shindo, T. Kondo, Evaporation behavior of hastelloy-X alloys in simulated very high-temperature reactor environments, Nucl. Technol. 66 (1984) 429–438.
[9] M. Shindo, W.J. Quadakkers, H. Schuster, Corrosion behavior of hightemperature alloys in impure helium environments, J. Nucl. Mater. 140 (2) (1986) 94–105.

[10] W.J. Quadakkers, H. Schuster, Thermodynamic ad kinetic aspects of the corrosion of high-temperature alloys in high-temperature gas-cooled reactor helium, Nucl. Technol. 66 (1984) 383–391.
[11] W.J. Quadakkers, H. Schuster, Corrosion of high-temperature alloys in the primary circuit helium of high-temperature gas-cooled reactors. 1. Theoritical background, Werkst. Korros. 36 (1985) 141–150.
[12] W.J. Quadakkers, Corrosion of high-temperature alloys in the primary circuit helium of high-temperature gas-cooled reactors. 1. Experimental results,Werkst. Korros. 36 (1985) 335–347.
[13] F. Rouillard, C. Cabet, K. Wolski, A. Terlain, M. Tabarant, M. Pijolat, F.Valdivieso, High temperature corrosion of a nickel base alloy by helium impurities, J. Nucl. Mater. 362 (2/3) (2007) 248–252.
[14] F. Rouillard, C. Cabet, K. Wolski, M. Pijolat, Oxide-layer formation and stability on a nickel-base alloy in impure helium at high temperature, Oxid. Met. 68 (3/ 4) (2007) 133–148.
[15] C. Cabet, J. Chapovaloff, F. Rouillard, G. Girardin, D. Kaczorowski, K. Wolski, M. Pijolat, High temperature reactivity of two chromium-containing alloys in impure helium, J. Nucl. Mater. 375 (2008) 173–184.
[16] J. Chapovaloff, D. Kaczorowski, K. Wolski, Influence of Al on the high temperature corrosion behaviour of Inconel 617 in VHTR primary coolant atmosphere, Mat. Sci. For. 595–598 (2008) 491–500.
[17] HSC Chemistry 5.11, Outokumpu Research Oy, Pori, Finland, 2002.
[18] H.M. Tawancy, High-temperature oxidation behavior of a wrought Ni–Cr–W– Si–La alloy, Oxid. Met. 45 (3/4) (1996) 323–348.
[19] R.E. Lobnig, H.P. Schmidt, K. Hennesen, H.J. Grabke, Diffusion of cations in chromia layers grown on iron-base alloys, Oxid. Met. 37 (1991) 81–93.
[20] D. Pop, K. Wolski, Surface segregation in Haynes 230 alloy, Appl. Surf. Sci. 253 (2006) 2244–2250.
[21] D.F. Lupton, Report JUL-1639 Kernforschungsanlage Jülich GmbH IRW, 1980.
[22] O. Kubaschewski, C.B. Alcock, Metallurgical Thermochemistry, fifth ed., Pergamon Press, 1979.
[23] S. Gossé, T. Alpettaz, F. Rouillard, S. Chatain, C. Guéneau, C. Cabet, Direct measurements of the chromium activity in complex nickel base alloys by high temperature mass spectrometry, Mater. Sci. For. 595–598 (2008) 975–985.
[24] S.N. Basu, J.W. Halloran, Tracer isotope distribution in growing oxide scales, Oxid. Met. 27 (3/4) (1987) 143–155.
[25] J. Gilewicz-Wolter, Study of iron oxidation in sulfur dioxide atmospheres by means of the 35S radioisotope, Oxid. Met. 11 (2) (1977) 81–90.
[26] P. Singh, N. Birks, Penetration of sulfur through preformed protective oxide scales, Werkst. Korros. 31 (1980) 682–688.
[27] L. Tomlinson, N.J. Cory, Hydrogen emission during the steam oxidation of ferritic steels: kinetics and mechanism, Corros. Sci. 29 (8) (1989) 939–965.
[28] G.B. Gibbs, Model for mild-steel oxidation in CO_2, Oxid. Met. 7 (3) (1973) 173– 200.
[29] I. Wolf, H.J. Grabke, P. Schmidt, Carbon transport through oxide scales on Fe–Cr alloys, Oxid. Met. 29 (3/4) (1988) 289–306.
[30] F. Rouillard, C. Cabet, S. Gossé, K. Wolski, M. Pijolat, Thermodynamic modelling of the destruction of the surface Cr_2O_3 on Alloy 230 in the impure helium atmosphere of a gas cooled reactor, Mater. Sci. For. 595-598 (2008) 429–430.[31] J. Philibert, in: Diffusion and Mass Transport in Solids, Monographie de Physique, Les Editions de Physique, 1985.

Figures captation

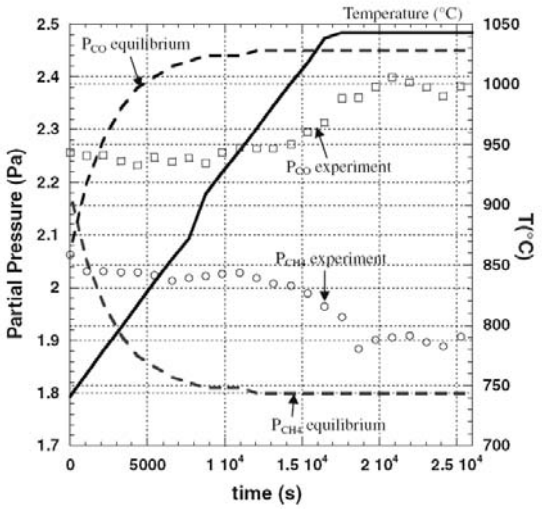

Figure 1: Outlet partial pressure of CO and CH_4 as a function of time during a blank test – ie without any samples – for an inlet helium mixture containing 2.5 Pa CO, 2.0 Pa CH_4, 20 Pa H_2 and 0.2 Pa H_2O. The theoretical partial pressures of CO and CH_4 calculated by thermodynamic equilibrium using HSC data [17] are represented on the graph.

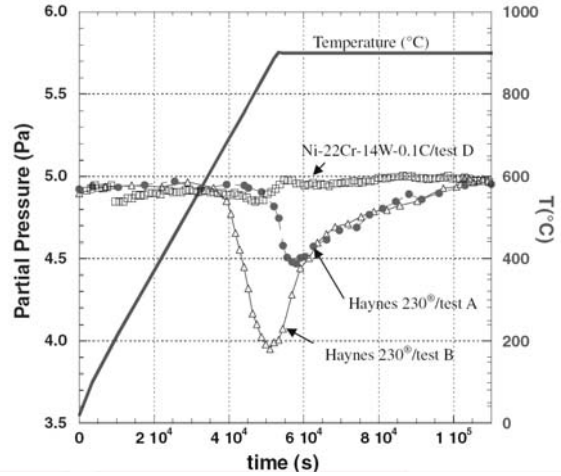

Figure 2: Temperature program and outlet partial pressure of CO as a function of time for Haynes 230® specimens during test A and B and for Ni–22Cr–14W–0.1C during test D (square dots).

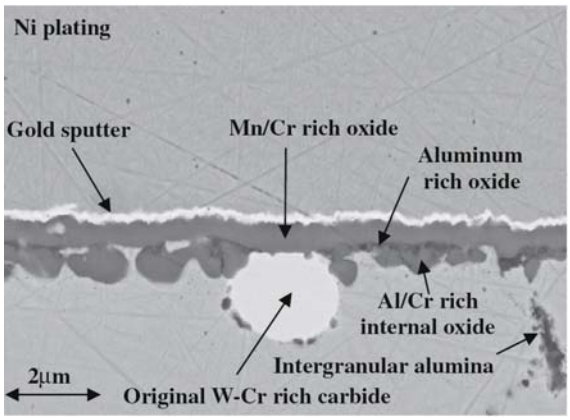

Figure 3: Cross section image of Haynes 230®obtained by FESEM with a backscattered contrast after test A (0.4 Pa H_2O).

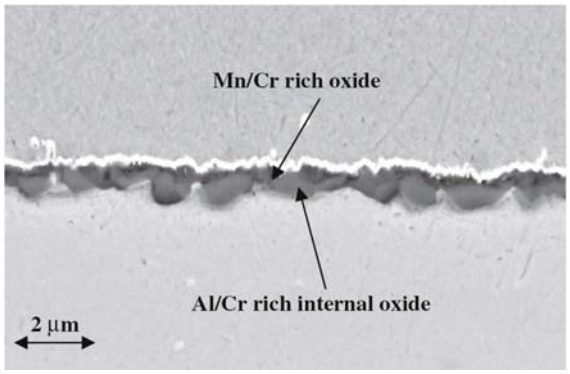

Figure 4: Cross section image of Haynes 230® obtained by FESEM with a backscattered contrast after test B (0.16 Pa H_2O)

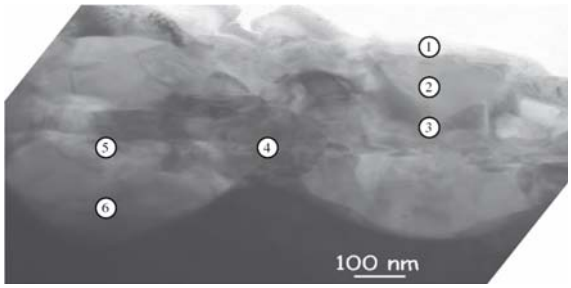

Figure 5: TEM image of the oxide layer formed on Haynes 230®after test A. The chemical composition of spots are given in Table 3.

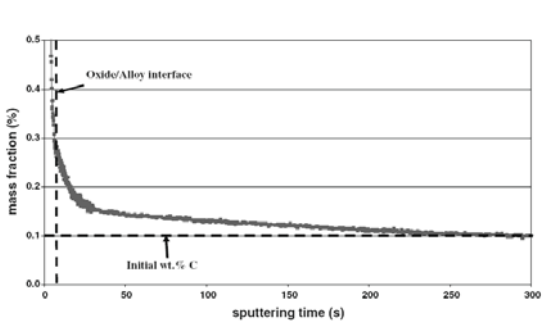

Figure 6: GDOES profile of carbon at the surface of Haynes 230® after experiment C (900 °C, 6 h); oxide surface is on the left hand side and bulk alloy on the right hand side.

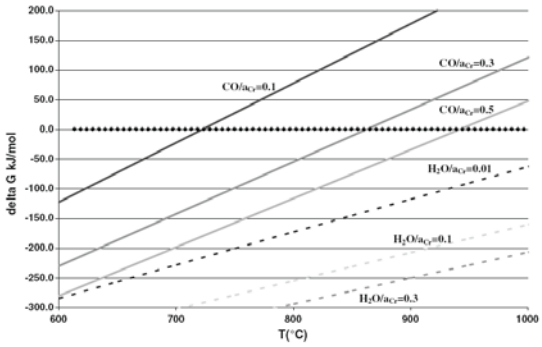

Figure 7: Standard free Gibbs Energy of formation [17] of Cr_2O_3 by H_2O or CO as a function of temperature and chromium activity in the alloy. P_{CO} = 5 Pa, P_{H_2O} = 0.2 Pa et P_{H_2} = 20 Pa. When oxidized by CO, the carbon transferred into the alloy is considered to be in equilibrium with $Cr_{23}C_6$ carbides formed in Haynes 230® [22] (see Ref. [30] for details). The standard states of each element are defined by their most stable form at 1 bar and 298.15 K.

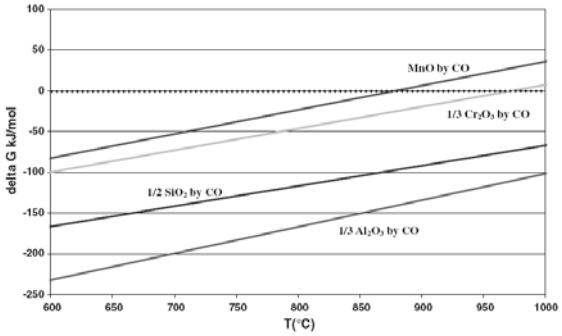

Figure 8: Standard free Gibbs energy of oxide formation [17] per mole O by H_2O or CO as a function of temperature under P_{CO} = 5 Pa, P_{H_2O} = 0.2 Pa, P_{H_2} = 20 Pa. The carbon transferred into the alloy by the reaction with CO is considered to be in equilibrium with $Cr_{23}C_6$ carbides formed in Haynes 230® [22]. Activities of elements are taken equal to their atomic fraction in Haynes 230® (ideal solution) except a_{Cr} which is taken approximately equal to 0.6 from activity measurements carried out on Haynes 230® [23]. The standard states of each element are defined by their most stable form at 1 bar and 298.15 K.

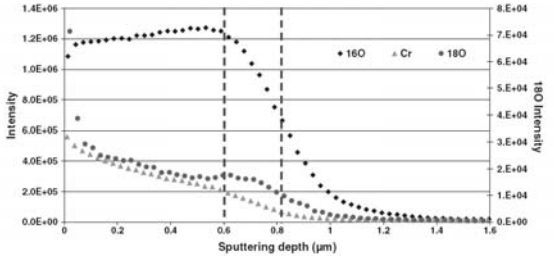

Figure 9: SIMS profiles (arbitrary units) of ^{16}O, ^{18}O and ^{52}Cr at the surface of Ni–22Cr–14W–0.1C after test E. ^{18}O intensity scale is on the right hand side.

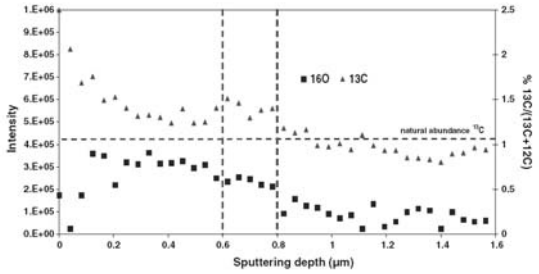

Figure 10: GDMS profiles (arbitrary units) of ^{13}C and ^{16}O at the surface of Ni–22Cr–14W–0.1C after test E. ^{13}C abundance (in %) is on the right hand side.

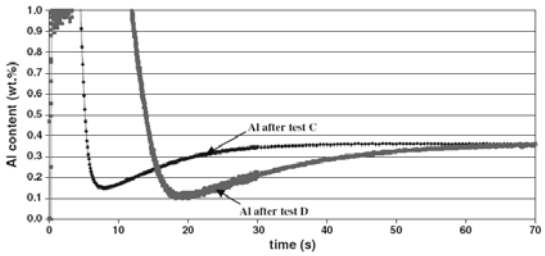

Figure 11: GDOES profiles of Al at Haynes 230® surface after test C (6 h, 900°C) and D (25 h, 900 °C).

Tables captation

	Ni	W	Cr	Mn	Fe	Ti	Si	Al	Mo	Co	C[b]	La
Haynes 230®[a]	Bal	14.7	22	0.5	1.3	0.1	0.4	0.4	1.3	0.2	0.105	0.005
Ni-22Cr-14W-0.1C[c]	Bal	14	22								0.103	

[a]By ICP – uncertainty: 3%.
[b]By LECO_.
[c]By weighing – uncertainty: 5%.

Table 1: Alloy composition (wt%).

Test	Alloy	Input gas composition [a] (Pa)				Linear gas flow rate (cm/s)	Temp. (°C)	Time(h)
		H_2	CO	CH_4	H2O[b]			
A	Haynes 230®	19.5 ±0.4	4.9 ± 0.1	2.1 ± 0.04	0.4	0.12	900	25
B	Haynes 230®	1.95 ±0.4	4.9 ± 0.1	2.1 ± 0.04	0.16	0.12	900	25
C	Haynes 230®	1.96 ±0.4	2.2 ± 0.04	1.9 ± 0.04	0.15	0.12	900	6
D	NicrWC	19.6 ±0.4	4.9 ± 0.04	2.1 ± 0.04	0.15	0.12	900	25
E/Step1	NicrWC	20.0 ±0.4	-		8-10	0.14	850	48
E/Step2	NicrWC	20.0 ±0.4	5.0 ± 0.1 ($^{13}C^{18}O$)		<0.01	0.14	850	48
F	NicrWC	20.0 ±0.4	5.0 ± 0.1		<0.1	0.14	900	25

[a] Detection limit: 0.01 Pa and accuracy: 2%.
[b] By a capacitive hygrometer with a detection limit of 10^{-4} Pa and an accuracy about ± 3°C

Table 2: Tests gas mixtures and conditions.

Analysed spot	*Cr*	*Al*	*Si*	*Ni*	*Mn*	*O*
1	*29*	-	-	*3*	*11*	*57*
2	*28*	-	-	*4*	*11*	*57*
3	*34*	-	-	*3*	-	*63*
4	*18*	*17*	*4*	*2*	-	*59*
5	*27*	*8*	*8*	*2*	-	*55*
6	*31*	*5*	-	*2*	-	*62*

Table 3: EDXS analyses in (at%).of different spots in the oxide layer presented in Figure 4

Carbon enrichment from Fig.5 (mol)	CO consumption from Fig.1 (mol)
4.45×10^6	4.20×10^6

Table 4: Comparison between the carbon transferred into Haynes 230® and the CO consumption during test C (in mol).

Test	Water vapour partial pressure (Pa)	Mean oxide layer thickness (µm)	Oxide layer thickness estimated by CO consumption (µm)	% of the oxide layer formed by CO reaction
A	4	600	110	~20
B	1.6	450	190	~55

Table 5: Fraction of the oxide layer formed by CO in test A and test B; mean oxide thickness from FESEM imaging and thickness of the oxide layer estimated from reaction with CO (based on Fig. 1).